Using coarse-grained molecular dynamics to rationalize biomolecule solubilization mechanisms in ionic liquid-based colloidal systems

Henrique Bastos, Ricardo Bento, Nicolas Schaeffer, João A. P. Coutinho and Germán Pérez-Sánchez*

[a]CICECO – Aveiro Institute of Materials, Department of Chemistry, University of Aveiro, 3810-1933 - Aveiro, Portugal;

*Corresponding author: gperez@ua.pt (Phone: +351-234-370200)

Abstract

Solubilizing agents are widely used to extract poorly soluble compounds from biological matrices. Aqueous solutions of surfactants and hydrotropes are commonly used as solubilizers, however, the underlying mechanism that determines their action is still roughly understood. Among these, ionic liquids (IL) are often used not only for solubilization of a target compound but in liquid-liquid extraction processes. Molecular dynamics simulations can shed light into this issue by providing a microscopic insight of the interactions between solute and solubilising agents. In this work, a new coarse-grained (CG) model was developed under the MARTINI framework for gallic acid (GA) while the CG models of three quaternary ammonium ionic liquids and salts (QAILS) were obtained from literature. Three QAILS were selected bearing in mind their potential solubilising mechanisms: trimethyl-tetradecylammonium chloride ($[N_{1,1,1,14}]Cl$) as a surfactant, tetrabutylammonium chloride ($[N_{4,4,4,4}]Cl$) as an hydrotrope, and tributyl-tetradecylammonium chloride ($[N_{4,4,4,14}]Cl$) as a system combining the characteristics of the other compounds. Throughout this hydrotrope-to-surfactant spectrum and considering the most prevalent GA species across the pH range, the solvation of GA at two concentration levels in aqueous QAILS solutions were studied and discussed. The results of this study indicate that dispersive interactions between the QAILS and GA are generally the driving force in the GA solubilization. However, electrostatic interactions play an increasingly significant role as the GA becomes deprotonated, affecting their placement within the micelle and ultimately the solvation mechanism. The hydrotropic mechanism seen in $[N_{4,4,4,4}]Cl$ corroborates recent models based on the formation of a hydrotrope-solute aggregates driven by dispersive forces. This work contributes to the application of a transferable approach to partition and solubilization studies using molecular dynamics, which could complement experimental assays and quickly screen molecular candidates for these processes.

Keywords: biomolecule modelling, drug solubilization, biomolecule extraction, ionic liquids, molecular dynamics, MARTINI model, hydrotropy

1. Introduction

The poor aqueous solubility of many biomolecules remains a major problem in many important applications such as drug development and delivery,[1] as well as their extraction[2] and purification[3]. Solubility enhancers such as surfactants, hydrotropes or co-solvents[4–6] are commonly used to promote the solubility of hydrophobic compounds in water. Surfactants are amphiphilic molecules able to self-assemble in diverse morphologies such as micelles and long-range ordered mesophases. Hydrotropes are also amphiphilic compounds, soluble in water, but unable to self-assemble due to a lower hydrophobic strength,[7] the target compound being solubilized by the formation of aggregates stabilized *via* solvophobic interactions.[8] A detailed understanding of the solubilization mechanisms in surfactant and hydrotrope systems remains poorly understood, in particular for charged molecules.[9] The main assumptions are based on the association of surfactant and solute, either in supramolecular structures such as micelles for micellar solubilization or short lived aggregates for hydrotropy.[10,11] Nonetheless, the lack of a specific point of differentiation between hydrotropes and surfactants remains, as there are hypotheses on the solubilization mechanisms that blur their distinction and a broad spectrum of molecules considered to fit these categories. This work aims to provide further material for this discussion by addressing the solvation in aqueous solutions of these agents.

Quaternary ammonium ionic liquids and salts (QAILS) are a class of compounds with the general formula $[N_{i,j,k,l}]X$ composed by a cationic organic nitrogen $[N_{i,j,k,l}]^+$ group and a counter anion X^-.[12] They cover a large range of compounds with very different properties, from simple salts (NH_4Cl) to ionic liquids ($[N_{4,4,4,4}]Cl$ or $[N_{4,4,4,14}]Cl$) or surfactants ($[N_{1,1,1,14}]Cl$). Many of the compounds on this family have amphiphilic properties, behaving as surfactants or hydrotropes, and generating colloidal systems in aqueous solutions.[13–16] For instance, cetyltrimethylammonium bromide ($[N_{1,1,1,16}]Br$, also known as CTAB) is a surfactant extensively used as a solubilizer of hydrophobic bio-active compounds,[17–19] – as well as an extractant[20,21] – whilst tetrabutylammonium-based QAILS ($[N_{4,4,4,4}]Cl$) is a hydrotrope capable of significantly increasing the solubility of poorly water-soluble drugs in aqueous solutions.[15,22,23]

The QAILS solubilization efficiency not only relies on the solvophobic but also on the electrostatic interactions, determined by the cation-anion and the solute-cation interactions. The latter is often neglected despite many biomolecules containing carboxylic moieties, which would

be deprotonated at biological pH values. Thus, the pH impact in the solubilisation and partition of biomolecules is of great relevance since the protonation state directly influences the electrostatic interactions.[24] The nature of the most common QAILS anions does not play an important role in the solubilization mechanism but can directly influence the phase separation.[25] A meaningful exception rises when the QAILS anion is an hydrotropic agent.[15,16] In this manner, QAILS cations can affect the solubilizing action depending on the alkyl-chain length and the cation asymmetry.[26] Finally, it must be noticed that QAILS have been widely used as surfactants but seldom as hydrotropes,[23,27–29] and thus this aspect is poorly studied and understood.

To shed light on the solvation mechanism in QAILS aqueous solutions, a comprehensive analysis of the interactions present on these systems is required. Computational chemistry methods can hasten this process and complement the experimental data. The characterization of solubility enhancers requires a good knowledge of the QAILS phase behaviour and the physico-chemical characteristics of the biomolecule. A multiscale strategy has been followed by many authors, from density functional theory (DFT) calculations[30–35] to classical Monte Carlo,[36–39] molecular dynamics (MD) simulations at both all-atom (AA) and coarse-grained (CG) levels[15,16,40–43] as well as dissipative particle dynamics (DPD).[44–46] The atomistic detail of DFT and AA-MD approaches fairly reproduce some experimental thermodynamic properties.[47] Unlike CG, atomistic models are not able to reproduce the QAILS phase behaviour due to time and size scale limitations.[48] Since the mechanism behind the solubilization of biocompounds depends on the surfactant and hydrotrope phase behaviour, the mesoscale level offered by CG-MD simulations is required.[27] CG dramatically reduces the computational requirement in the MD simulation by including groups of atoms with similar physico-chemical characteristics into one interaction center. A proper AA-to-CG mapping and the CG interaction energy parameters are essential to develop a new CG model. Marrink et al. developed the transferable MARTINI CG model for molecular systems, including many biomolecules.[49] The MARTINI framework comprises a generic energy matrix of interactions which includes four main flavours – polar, apolar, non-polar and charged moieties – with different subtypes each depending on the degree of polarity or the implicit hydrogen bonding capabilities.[49] The MARTINI model was widely and successfully applied in diverse systems including many QAILS as well as different biomolecules.[42,45,50]

In this work, a CG approach based on the MARTINI force field was developed to discuss the solvation of gallic acid (GA). Herein, CG-MD simulations were carried out to further understand

the solvation mechanism of GA in three QAILS aqueous solutions, tackling the micellar solubilization to hydrotropy. Thus trimethyl-tetradecylammonium chloride ([$N_{1,1,1,14}$]Cl), tetrabutylammonium chloride ([$N_{4,4,4,4}$]Cl) and tributyl-tetradecylammonium chloride ([$N_{4,4,4,14}$]Cl) QAILS were selected under dilute conditions to cover the surfactant micellar and hydrotropic solubilization mechanisms. The GA is a phenolic acid with antioxidant activity and widely used as a probe/reference molecule in various drug partition assays.[51,52] The GA-CG model developed in this work improves the previous computational attempts reported in the literature, capturing in more detail, its physico-chemical characteristics.[42,45] Moreover, the GA-CG model was created to consider different protonation states which is crucial to capture the solute charge, resulting from the pH effect, in the solvation. A multiscale strategy was followed to develop the GA-CG model based on AA-MD simulations.[41,53,54] This work paves the way to enhance our knowledge on the molecular interactions involved in the solvation of biomolecules in QAILS aqueous solutions. In turn, it may help in designing more and highly efficient solubility-enhancing systems for a wide array of substances.

2. Methodology

2.1 Simulation details

MD simulations were carried out with the GROMACS package[55] (version 5.1.5) under a NpT ensemble by adopting the leapfrog algorithm[56] to integrate the equations of motion for at least 0.5 μs with a 10 fs time step. The non-bonded interactions comprised the Lennard-Jones (LJ) potential and Coulombic terms, both with a cut-off radius of 1.2 nm. The van der Waals (vdW) potential force-switch modifier was chosen allowing the energy to decay smoothly towards zero from 0.9 to 1.2 nm. The long-range electrostatic interactions were evaluated using the Particle-Mesh-Ewald (PME)[57] and the potential-shift functions as modifiers. The temperature was fixed to 298K using the velocity-rescaling thermostat.[58] An isotropic pressure coupling was considered using the Parrinello-Rahman barostat[59] to control the pressure in both, the equilibration and production runs at 1 bar. Bonded interactions encompassed bond stretching, angle bending and dihedral torsion terms where bonds were constrained using the LINear Constraint Solver (LINCS).[60] Triclinic simulation boxes were selected with periodic boundary conditions in all directions and random initial configurations.

The simulation protocol was as follows: an initial energy minimization step using the steepest descent algorithm to avoid close contacts between neighbour atoms followed by a short equilibrium steps in the NVT and NpT ensembles, consecutively, prior the production run. The system evolution was checked by visual inspection and the total energy was monitored to confirm whether the thermodynamic equilibrium is attained. The CG models for $[N_{1,1,1,14}]^+$ and $[N_{4,4,4,14}]^+$ were selected based on analogous systems previously developed[50,61] as illustrated in **Figure S1** in the Supporting Information. The $[N_{4,4,4,4}]Cl$ CG model was adapted based on the mapping of the polar head for $[N_{4,4,4,14}]Cl$. Overall in these systems, the total number of QAILS molecules was 500 and two GA concentrations comprising 25 and 200 GA molecules, respectively, were taken into account as well as three different GA protonation states. Thus, the two GA concentrations were considered based on the GA solubility limit in water – 11.9 mg/mL at 298K[62] – one below (from 2.33 mg/mL to 3.58 mg/mL) and one above (from 18.94 mg/mL to 28.62 mg/mL) labelled as low and high, respectively. The three GA protonation states corresponds to the most prevalent species in the speciation spectrum as shown in **Figure 1**, covering the full pH range. The description of each protonation state was based on the selection of different bead types for the relevant groups. The protonated GA molecule was labelled as Prot. GA, the one with the carboxylic moiety deprotonated was named Deprot. GA (-1) and the one with both the carboxylic and the two hydroxylic moieties deprotonated was designated as Deprot. GA (-3).

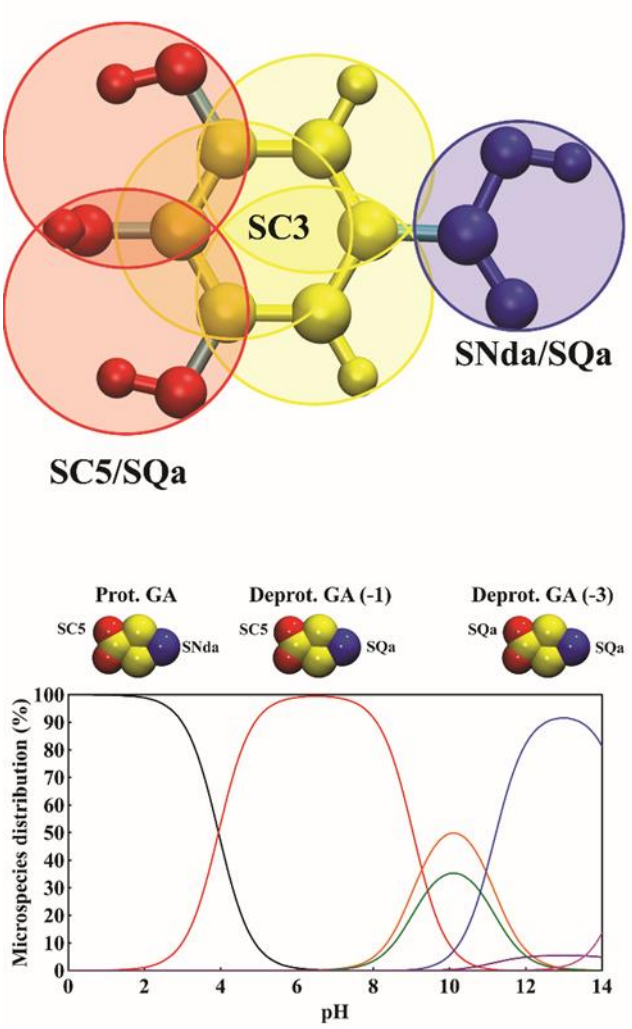

Figure 1. Coarse-grained mapping scheme for GA used in this work (top). Three different models based on distinguished ionization states were developed as these represent the three most prevalent species throughout the pH spectrum[63] (bottom). In the speciation spectrum, Prot.GA is in black, Deprot. GA (-1) in red and Deprot. GA (-3) in blue. The other colours depict less prevalent species. In all cases, the aromatic ring was set as moderately apolar (SC3) bead. The carboxylic acid moiety ranged from nonpolar (SNda) to charged (SQa) when in the Prot. and the Deprot. (-1) states, respectively. Similarly, the hydroxylic groups were described as weakly apolar (SC5) in the two former states and as charged (SQa) in the Deprot. (-3) ionization.

Polarizable water (PW) was selected to capture the dipole effect and allow an adequate screening of electrostatic charges. The PW bead entails three real water molecules as illustrated in **Figure S1**. The Q_a and Q_d beads were chosen for chloride and sodium counter ions, respectively,

and include the first hydration layer with six implicit water molecules according to the MARTINI model[49] as depicted in **Figure S1**. For each system, the number of QAILS, GA, ion pairs, PW beads and the simulation time are reported in **Table S1**.

The simulation outputs were visualized with the Visual Molecular Dynamics (VMD) package.[64] The GROMACS analysis tools were used to obtain the radial distribution functions (RDF). The density profiles were obtained by using an in-house cluster-counting code[65] based on the Hoshen-Kopelman algorithm[66] when spherical aggregates were present, otherwise the GROMACS *gmx density* tool was used. The Trajectory Analyzer and VISualizer (TRAVIS) tool[67] was applied to obtain the spatial distribution functions (SDF).

2.2. Coarse-grain model development and validation of gallic acid

The GA-AA molecule structure was taken as a reference to map the CG version. The GA-AA forcefield parameters were taken from the OPLS-AA forcefield[68] while water molecules were represented by the SPC/E model[69]. The GA atomic partial charges were obtained by DFT optimization in the gas-phase at the B3LYP[70]/6-31G* level of theory with the CHELPG option[71] using the Gaussian 09 package[72] and are displayed in **Figure S2**. A visual representation of electrostatic potential mapped of the electron density is also available as a guideline in **Figure S3**.

The new GA-CG model required several mappings and parameterization attempts prior to find a good agreement with the AA model. **Figure 1** shows the final GA-CG mapping schemes, considering the three different ionization states tested in this work which were denominated as Prot. (fully protonated molecule, pH < 4.44),[73] Deprot. (-1) (intermediate ionization, 4.44 < pH < 8.45)[73] and Deprot. (-3) (fully ionized molecule, pH > 8.45). Despite the pH has an important role in the phase behaviour, the pH effect was neglected in previous GA-CG simulations with surfactants and hydrotropes.[24,74–76] Thus, the pH was carefully considered in this work by developing several GA-CG mappings which corresponds to the most relevant ionization states.

In our model, a 3:1 mapping and the small CG bead versions of MARTINI labelled as "S" beads were selected. The "S" beads reduces the LJ well-depth (ε) in 75% and the sigma is decreased to 0.43 nm to reproduce properly the geometry of small ring molecules.[49] Therefore, the aromatic ring was described by three moderately apolar SC3 beads. The carboxylic acid region was characterized as follows; nonpolar (half polar/apolar) with SNda when protonated whereas

SQa was selected when the GA is deprotonated. The subscripts indicate the hydrogen bonding capabilities, d = donor, a = acceptor and da = both. The hydroxylic groups were reproduced from weakly apolar SC5 beads in Prot./Deprot. (-1) states to charged SQa beads in the Deprot. (-3) state.

The Prot. and Deprot. (-1) systems were validated according to AA-MD results. The RDF between different regions of the GA and water were evaluated. **Figure S4** shows the RDF between the carboxylic acid group and water since displays the main role in the interaction with water. A good qualitative agreement was found between both AA and the CG models. The AA and CG Prot. GA RDFs displayed a similar pattern with a weak interaction with water. This interaction was increased in both, AA and CG, in the Deprot. GA versions where the two solvation shells of the carboxylic group were reproduced in the AA and CG models. The CG-GA RDFs overestimate the distances compared with the AA version caused by the CG beads used in the calculation. The water CNs highlight the fact that Deprot. GA is more solvated compared with the Prot. GA as shown in **Figures S4** and **S5**. The correlation between both profiles indicate that the CG model should represent properly interaction of the carboxylic acid group (and similar ones) with water, mainly due to ion-dipole and hydrogen bonding interactions. **Figure S5** displays the SDF which provide a visual insight not only on the hydration of GA (blue) enhanced in the Deprot. GA but on other interactions with surrounded GA molecules. The SDFs clearly demonstrate the π-π interactions (green) established between GA molecules which hint possible cation-π interactions with other molecules such as the cationic ammonium QAILSs used in this work.

Our GA-CG models differs from previous works[42,45] motivated by the need of an increased polarity among different regions of the molecule. For instance, Xiang and colleagues[45] used a similar GA-CG mapping but the model failed to capture the polarity differences of each GA region. The model by Chatzidaki et al.[42] suffered a similar issue since the GA was described with only three beads. Two SP4 MARTINI beads comprised most of the aromatic ring and the hydroxylic regions whereas the intermediate polar SP3 was used for the carboxylic acid group.

3. Results and discussion

3.1. GA solvation in aqueous surfactant solution

The solvation of GA in aqueous QAILS solutions is discussed based on three parameters: the QAILS nature, the GA protonation state, and the GA concentration. In this study, a spectrum of

solubilization mechanisms was covered, ranging from micellar solubilization to hydrotropy. $[N_{1,1,1,14}]Cl$ fits the former[77] while $[N_{4,4,4,4}]Cl$ follows the latter.[15] $[N_{4,4,4,14}]^+$ shares structural properties with the $[N_{1,1,1,14}]^+$ due to the alkyl-chain length and the $[N_{4,4,4,4}]^+$ by the bulky ammonium polar head (**Figure S1**). Three GA protonation states and two GA concentrations were considered; one below the GA solubility limit in water (from 2.33 mg/mL to 3.58 mg/mL) and one above (from 18.94 mg/mL to 28.62 mg/mL) referred to as low and high, respectively.

The discussion initially focuses in the higher GA concentration for clarity, as the overall phase behaviour is more evident. The MD snapshots after at least 0.5 μs of simulation time for all systems are depicted in **Figure 2**. A visual inspection indicates the distinct behaviour of the three QAILS, and that the solvation of GA within the QAILS aggregates decreased in all systems when triply deprotonated. Overall, although the solvation of GA seems similar when considering both GA concentrations, this variable significantly affected the phase behaviour of the system. Thus, the following observations were more noticeable in the high GA concentrated systems. The $[N_{1,1,1,14}]Cl$ system yielded stable micellar aggregates for all tested conditions. In contrast, the $[N_{4,4,4,14}]Cl$ system presents a clear phase transition from spherical micelles for Prot. GA to rod-like aggregates for Deprot. GA (-1) to finally phase separation for Deprot. GA (-3), when GA concentration was higher. This phase separation was driven by the larger extent of dispersive interactions between the QAIL and GA, due to the former having larger alkyl chains in the cation polar head, and consequently, a more non-polar character. Such a drastic transition was also promoted by the electrostatic interactions between a GA with a higher deprotonation degree and the positive QAIL. The micellar profile for $[N_{1,1,1,14}]Cl$ and $[N_{4,4,4,14}]Cl$ – except the Deprot. GA (-3) that shows phase separation – indicates that the $[N_{4,4,4,14}]Cl$ bulkier cation polar head rendered its micelles a 'looser character', highlighting their susceptibility to dispersive interaction effects. The behaviour of the hydrotrope $[N_{4,4,4,4}]Cl$ is addressed in the following sections, as well as the solvation of GA when using each of the three QAILS.

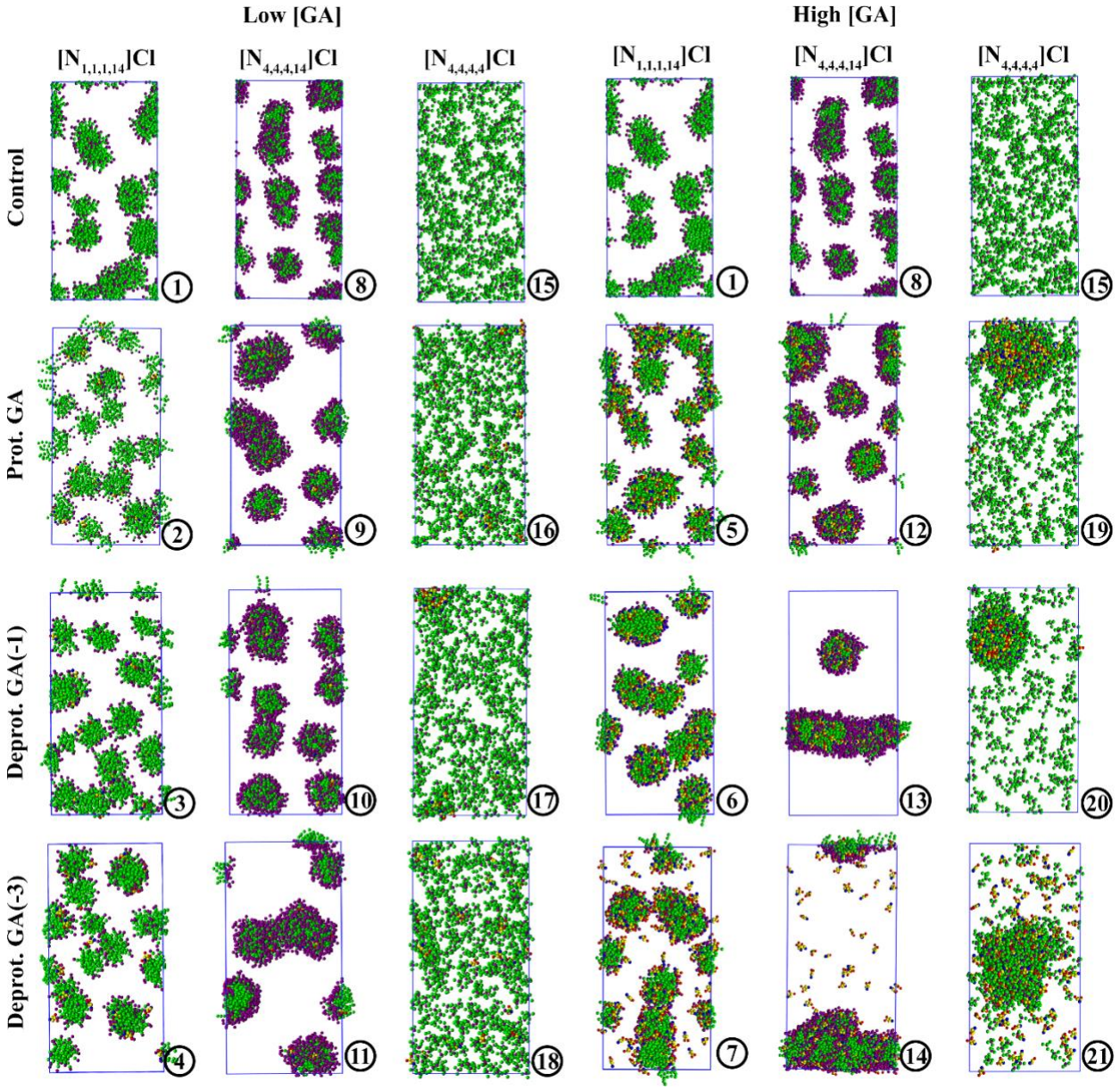

Figure 2. Snapshots of QAILS + GA systems (**Table S1**: 1-21) after the production runs. Each number on the bottom right corner of each snapshot indicates the system number according to **Table S1**. Control systems are QAILS aqueous solutions. QAILS cations polar heads are represented in purple and their alkyl chains in green. For GA, the carboxylic acid group is coloured in blue, the aromatic ring in yellow and the hydroxyls in red. Water, chloride and sodium molecules were removed for clarity.

3.1.1 GA solvation in [$N_{1,1,1,14}$]Cl

The density profiles of the [$N_{1,1,1,14}$]Cl aggregates obtained in the simulations are depicted in **Figure 3** and provide information on the location and orientation of GA in [$N_{1,1,1,14}$]Cl aqueous solutions. The cluster counting code used is not adequate when prolate-shaped structures are present and thus cannot be applied to the analysis of the [$N_{4,4,4,4}$]Cl or [$N_{4,4,4,14}$]Cl systems. The [$N_{1,1,1,14}$]Cl micelle density profiles show the arrangement of GA in the micelle and how the GA solvation in the micelle depends on the GA speciation. The GA carboxylic group is denoted by the red curve in **Figure 3** whilst the aromatic ring and hydroxyl group are grouped together and represented by the orange curve. When fully protonated (**Figure 3A**), GA is completely immersed in the micelle core as evidenced by the orange and red peaks in the inner of the micelle surface (purple curve). Furthermore, no specific arrangement of GA within the micelle was observed, ruling out potential π-π interactions between neighbouring GA molecules. This is the expected behaviour for the solvation of non-charged hydrophobic molecules in micellar systems. As the pH increases and the GA becomes charged the behaviour changes noticeably. When the carboxylic acid moiety is deprotonated, GA molecules become perpendicularly aligned with $[N_{1,1,1,14}]^+$ micelle surface (**Figure 3B**) as it can be noticed by the larger distance between the peaks corresponding to the carboxylic and aromatic moieties, seen by comparing the distance between the arrows in **Figures 3A and B**. When the deprotonation state of GA further increases to -3, the GA molecules are now present at the micelle surface as shown in **Figure 3C**. Since both carboxylic and hydroxyl moieties are deprotonated, interactions between the anionic Deprot. GA (-3) and the cationic head groups at the micelle surface are enhanced. In fact, an ion-exchange may be occurring in which a new QAILS is formed, using the deprotonated GA as the anion rather than the chloride (**Supporting Information**). The overlap of the GA peaks (red and orange curves) with the surfactant head groups (purple) suggests that Deprot. GA (-3) nearly adopts a flat conformation on the outer micelle surface. The [$N_{1,1,1,14}$]Cl phase behaviour and the GA solvation on these systems were the same in the systems with a lower GA concentration, although less visible in the latter as illustrated in **Figure 2**. For increased clarity, a scheme of the different orientations of GA molecules, depending on their protonation state, on $[N_{1,1,1,14}]^+$ micelles is depicted in **Figure 4**.

The work developed by Schwarz et al. demonstrated that cationic surfactant solutions, compared to other types, resulted in a higher percentage of GA partitioning to the surfactant phase.[78] Moreover, they also showed that with increasing pH, the GA had its presence reduced in the surfactant phase and increased in the aqueous one.[78] These observations can be now explained with the results obtained in this work as resulting from the GA transition from the micellar interior to the micelle-water interface as its deprotonation increased.

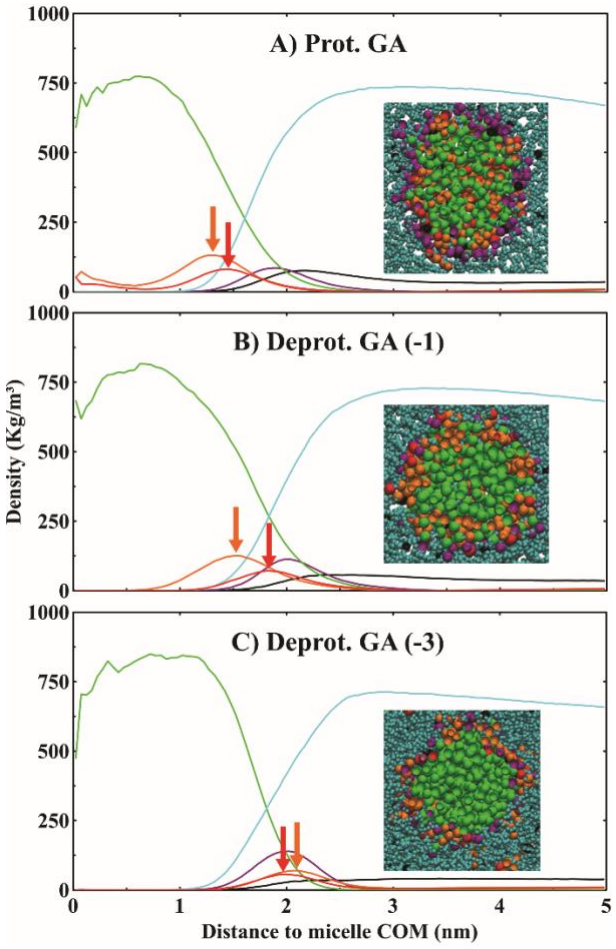

Figure 3. Density profiles for the aqueous systems (**Table S1**: systems 5-7) of $[N_{1,1,1,14}]^+$ and Prot.GA (A), Deprot. GA (-1) (B) or Deprot GA (-3) (C). Each group is plotted against their distance to the micelle center of mass (COM). Close-ups of a representative micelle are provided as an inset. QAILS cation polar heads are shown in purple and alkyl tail atoms in green. GA was divided in a carboxylic group coloured in red whereas the rest of the molecule was coloured in orange. Chloride ions were represented in black and water in cyan. The density peaks for GA groups were highlighted with black arrows.

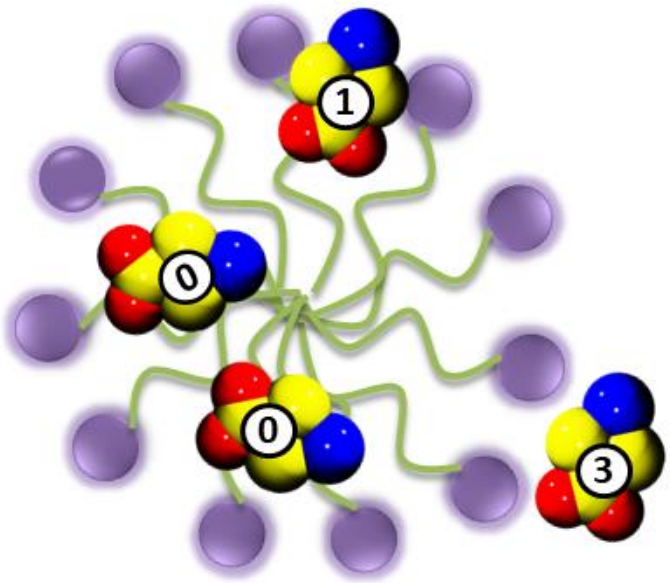

Figure 4. Schematic representation of a $[N_{1,1,1,14}]^+$ micelle and the different orientations of GA molecules towards it, depending on the pH of the solution. The micelle surface is depicted by the purple limits, while its core is coloured in green and a black dot illustrating the micelle center. GA molecules are represented by a coarse-grained description, in which the carboxylic acid group is in blue, the aromatic ring in yellow and the hydroxyls in red. Prot. GA, Deprot. GA (-1) and Deprot. GA (-3) are distinguished by the respective net charge (0, -1 and -3) in the center of the GA molecule.

3.1.2 GA solvation in $[N_{4,4,4,14}]Cl$

Unlike what can be observed in **Figure 2** for the $[N_{1,1,1,14}]Cl$ system, the GA concentration has a marked influence on the phase behaviour of $[N_{4,4,4,14}]Cl$. At a GA concentration below its solubility limit in pure water, the QAILS remained in a micellar regime (**Figure 2**), also evidenced in the micelle density profiles shown in **Figure S6** for all GA protonation states. However, when the GA concentration is increased in the $[N_{4,4,4,14}]Cl$ system, it evolves towards a phase separation (**Figure 2**). Regardless of the GA concentration, the GA orientation in $[N_{4,4,4,14}]^+$ micelles is similar to that observed with $[N_{1,1,1,14}]Cl$ as shown in the density profiles displayed in **Figure 5** and **Figure S6** for high and low GA concentrations respectively. For the systems with higher GA concentration, differences in the GA protonation state were observed not only in terms of phase transition but also for the orientation of GA. The initial micellar state, with Prot.GA, changed

noticeably when compared to the Deprot. GA (-1). Prot.GA is located deep inside the $[N_{4,4,4,14}]Cl$ micelle core as illustrated in **Figure 5B** (the GA density coloured in orange and red was increased compared with the Prot. GA shown in **Figure 5A**). Moreover, the larger distance between the two peaks indicates a more defined orientation of GA in the QAILS micelles (**Figure 5B**). In the case of triply deprotonated GA, a phase separation of the $[N_{4,4,4,14}]^+$ surfactant was observed with all $[N_{4,4,4,14}]^+$ coalescing in one large aggregate. The Deprot. GA (-3) was mainly located at the interface of the aggregate. In this case the same ion-exchange hypothesis mentioned in the previous section could also apply, although in a different extent (**Supporting Information**). Although our results point toward a phase transition of the system with Deprot. GA (-1) and eventually phase separation in the Deprot. GA (-3) system, it is difficult to fully ensure this at this simulation scale. Indeed, such surfactants are known to form worm-like bicontinuous aggregates, like the one in Deprot. GA (-1), before phase separation.[79,80] Thus, this is likely the occurrence showed in these systems, as our results indicate. Overall, when $[N_{4,4,4,14}]^+$ micelles are present in the system the localization and orientation of GA molecules is similar to that depicted for the $[N_{1,1,1,14}]^+$ (**Figure 4**).

A difference in phase behaviour was clearly induced by the QAILS nature. Thus, the interactions between QAILS and GA are affected by the surfactant polar head volume since this is the only difference between $[N_{1,1,1,14}]Cl$ and $[N_{4,4,4,14}]Cl$ QAILS. The $[N_{1,1,1,14}]Cl$ is similar to the CTAB surfactant and other cationic surfactants. They have their self-aggregation promoted by the electrostatic balance of repulsion between charged head groups and attracted solvophobic regions.[81,82] On the other hand, in the $[N_{4,4,4,14}]Cl$, the increased volume of the non-polar groups in the polar head screen the head-group density charge, rendering it closer to a non-ionic surfactant behaviour.[79] The phase transition from a micellar to a phase separation (**Figure 2**) can thus be explained by the progressive aggregation, due to their more hydrophobic character, of the QAILS head-groups.[83,84] The deprotonation of GA also promotes the electrostatic interaction between the QAILS and GA, further enhancing this phenomenon. In this case, the variation of the deprotonation degree of GA seems to interfere with the overall phase behaviour favoured by the head group size difference of $[N_{4,4,4,14}]^+$. Contrarily, the micellar stability of the $[N_{1,1,1,14}]Cl$ was not significantly affected by the GA protonation state.

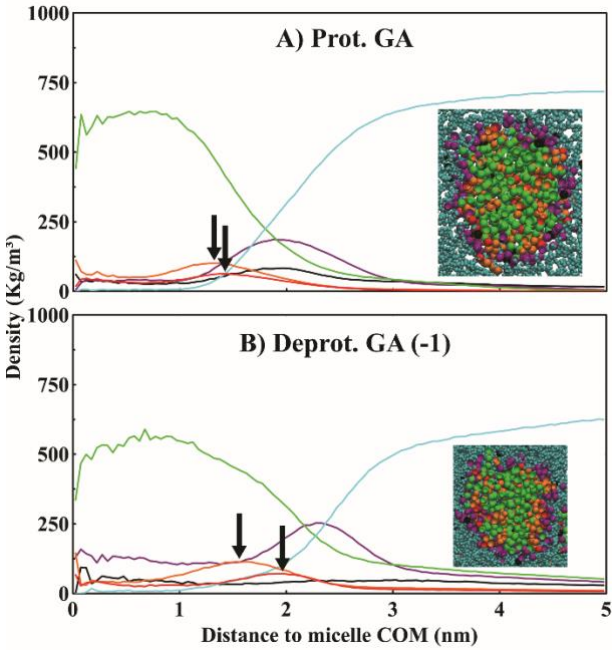

Figure 5. Density profiles for the aqueous systems (**Table S1**: systems 12, 13) of $[N_{4,4,4,14}]^+$ and Prot.GA (A) and Deprot. GA (-1) (B), using the micelle center of mass (COM) of QAILS micelles as a reference. Close-ups of a representative micelle are provided as an inset. Colour code is the same as in **Figure 3**. The density peaks for GA groups were highlighted with black arrows.

3.1.3 GA solvation in $[N_{4,4,4,4}]Cl$

A different scenario is observed in the $[N_{4,4,4,4}]Cl$ because it does not self-assemble in aqueous solution, as shown in the **Figure 2** Control. The GA solvation is discussed based in the simulation box density profiles shown in **Figure 6** and by visually inspecting the simulation snapshots displayed in **Figure 2**. As mentioned the $[N_{4,4,4,4}]Cl$ was fully dispersed in aqueous solution in absence of GA or even at low GA concentration as shown in **Figure 2**. However, when the GA concentration is increased, large clusters were observed not only for Prot. GA, as expected, but for all three GA protonation states. The $[N_{4,4,4,4}]$-GA cluster sizes at high GA concentration were estimated to range from 74 Å in Prot. GA to 104 Å in Deprot. GA (-1) and 118 Å in the Deprot. GA (-3).

The hydrotropy mechanism has been discussed for decades with recent works by Shimizu and co-workers questioning the classical views of hydrotropy.[9,85,86] In these works, they showed that

the interactions between the hydrophobic solute and the hydrotrope, whenever preferred over solute-water, can drive the hydrotrope aggregation enhancing the solute solubility.[9,85,86] Indeed, the interactions between $[N_{4,4,4,4}]^+$ and GA seem preferred over GA and water in the systems with Prot. GA and Deprot. GA (-1). This is in agreement with the results of a recent experimental work that demonstrate the hydrotrope-solute association depending on the apolarity of both compounds.[11] When the GA becomes more polar, by increasing its deprotonation, the GA-water interactions increase and compete with the dispersive interactions that drive the hydrotropic solubilization. This explains why, at low GA concentration, the system with Deprot. GA (-3) does not form clusters.

Figure 2 suggests that all systems with a high concentration of GA induce a phase separation of $[N_{4,4,4,4}]^+$ from water, as confirmed in the density profile of **Figure 6**. Although this phenomenon has not been experimentally observed for this system, phase separation resulting from the enhanced solubility in hydrotropic systems was previously observed for vanillin with ionic liquids.[15] The results here reported support and help to explain this behaviour. The formation of the aggregates resulting from the preferential interaction of the solute and hydrotrope may, in certain cases, lead to a destabilization of the liquid phase inducing the system towards a phase separation.

This phase separation in the system under study was observed for all GA protonation states. However, as suggested above, while for Prot. GA and Deprot. GA (-1) we may still observe the formation of aggregates, typical of hydrotropy, the system with Deprot. GA (-3) is far more complex and dominated by electrostatic interactions between the two salts in solution and it cannot be rationalized in the same way as the two other systems. Indeed, as the deprotonation degree of GA was increased, the resolution of this phase separation was clearer, as noted by the more defined peaks of both water and the hydrotrope in **Figure 6,** and the Deprot. GA (-3) system resulted in a single and larger cluster of $[N_{4,4,4,4}]^+$ (**Figure 2**). These indicate that different underlying mechanisms, depending on the presence of GA as neutral or as a highly charged ion (deprotonated), are taking place.

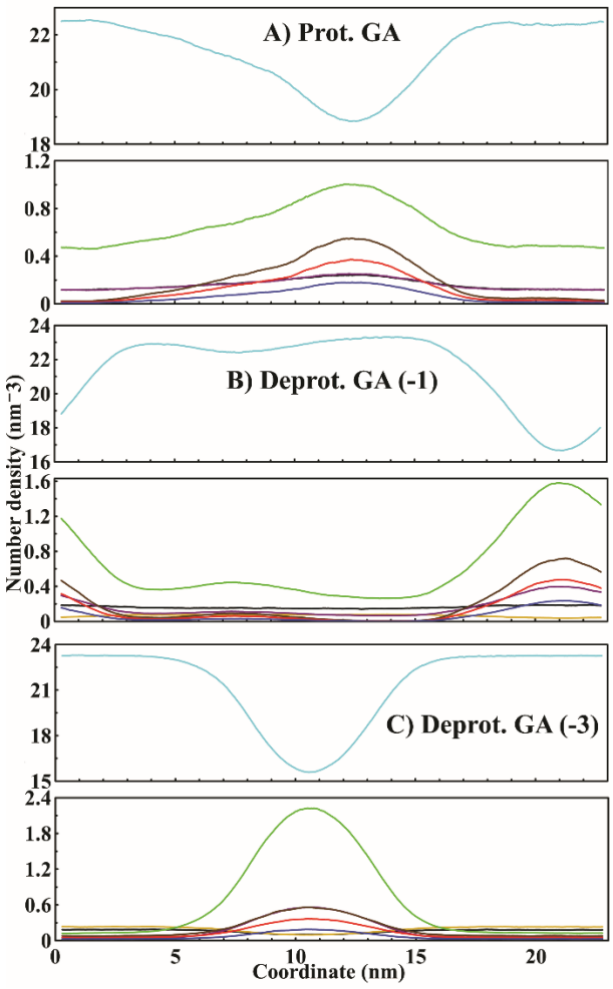

Figure 6. Density profiles for the aqueous systems (**Table S1**: systems 19-21) of $[N_{4,4,4,4}]^+$ and Prot.GA (A), Deprot. GA (-1) (B) or Deprot. GA (-3) (C). The density profile was obtained along the *z*-axis. QAILS cation polar heads are shown in purple, tail atoms in green. GA was split in the three different bead types: indigo for the carboxylic acid moiety, red for the hydroxyls and brown for the aromatic ring. Chloride ions were represented in black, sodium ions in yellow and water in cyan.

3.2 GA effect on micelle swelling

The discussion above revealed that the mutual QAILS and GA interactions affect both the GA solvation and the QAILS phase behaviour. This was particularly noticeable in systems with bulkier QAILS, namely $[N_{4,4,4,14}]Cl$ and $[N_{4,4,4,4}]Cl$. The final simulation snapshots at higher GA concentration (**Figure 2**) indicated that besides the phase transitions observed in $[N_{4,4,4,14}]Cl$ and $[N_{4,4,4,4}]Cl$, the $[N_{1,1,1,14}]Cl$ behaviour also changes with the GA deprotonation degree. Thus, GA

affects the systems through the concentration and deprotonation degree. Comparison between **Figure 2** shows that for micellar systems – $[N_{1,1,1,14}]Cl$ and Prot.GA with $[N_{4,4,4,14}]Cl$ – the increase in the GA concentration may lead to QAILS micelle swelling.

In $[N_{1,1,1,14}]Cl$ systems, a stable micellar QAILS phase remains in presence of GA. However, individual micelles seem to interact and enlarge with increasing GA charge density. A similar scenario occurs with $[N_{4,4,4,14}]Cl$, albeit even more noticeable, as eventually it leads to a phase separation. Combining this with the GA solvation inside these QAILS micelles, in Prot. GA and Deprot. GA (-1) states, micelle swelling can be considered. The average aggregation number (AN) of micelles was obtained to address this change in micelle size (**Table S1**). In case of stable micellar solutions, in $[N_{1,1,1,14}]Cl$ the ANs are also available in **Table 1**. When non-micellar solutions took place, the distance between each GA and the micelle center of mass was obtained through RDF profiles to corroborate the absorption of GA by QAILS micelles (**Figure 7**). The penultimate apolar C1 bead (adjacent to the end of the QAILS cation tail) was selected as the micelle center reference. It must be highlighted that the CG bead overlap inherent to the CG mapping processes, as well as the QAILS arrangement as a part the micelle, could induce some inaccuracy in selecting the actual micelle core center.

Table 1. Average aggregation numbers (ANs) obtained in the $[N_{1,1,1,14}]Cl$ micellar systems (**Table S1**: systems 1-12).

Sim.	QAILSs	[QAILS] (wt. %)	[GA] (wt. %)	GA net charge	AN
1		10.02	0	-	38
2		9.99	0.29	0	28
3		10.01	0.29	-1	29
4	$[N_{1,1,1,14}]Cl$	10.00	0.28	-3	33
5		9.79	2.28	0	45
6		9.66	2.24	-1	56
7		9.37	2.13	-3	56
8		10.02	0	-	45
9		10.00	0.20	0	100
10	$[N_{4,4,4,14}]Cl$	10.01	0.20	-1	63
11		10.08	0.20	-3	125
12		9.86	1.60	0	71

The AN corroborates this hypothesis (**Table 1**) particularly when considering systems with higher GA concentration. The addition of a low GA concentration in $[N_{1,1,1,14}]Cl$ systems did not result in micelle swelling, since the ANs were lower than the system without GA, AN ~ 38 (**Table 1**). For the ones with $[N_{4,4,4,14}]Cl$, the micelles were significantly enlarged from an AN of around 45 to 100 and more in some cases (**Table 1**), partially a result of a bulkier QAILS head. The addition of only 10 GA molecules were not able to disrupt the micellar structure followed by a swell process, while the latter occurred with 200 GA. Moving to higher GA concentrated systems, while those with Prot. GA showed an average of AN ~ 45 for $[N_{1,1,1,14}]^+$, for those with both Deprot. GA (-1) and Deprot. GA (-3) the AN increased to 56 (**Table 1, system 5-7**). The CNs inset in **Figure 7** indicate a movement away from the micelle center especially for the bulkier GA regions as it became more deprotonated – the aromatic ring and the hydroxylic moieties – which supports the swelling of the micelle through this pH effect. Both ANs and CNs for $[N_{4,4,4,14}]Cl$ systems for the GA were higher than those with $[N_{1,1,1,14}]Cl$. When considering Prot. GA, the $[N_{4,4,4,14}]Cl$ system exhibited an AN of 71, with a larger difference than the two control QAILS systems, indicating that is was a result of other factor than just the bulkier nature of $[N_{4,4,4,14}]Cl$. The more hydrophobic polar head of that shields the charge, allowing more disperse interactions between the two compounds. for solutions with Prot. GA (**Table 1, system 12**), resulting in a more distributed presence of GA inside its micelles. This could also justify the higher CNs registered for $[N_{4,4,4,14}]Cl$ when considering Deprot. GA (-1), a system already progressing towards phase separation. From previous density profiles and visual inspections, it is still possible to infer that the single micelle with Deprot. GA (-1) was enlarged. For $[N_{1,1,1,14}]Cl$ systems, larger $[N_{1,1,1,14}]^+$ micelles were observed throughout all GA states. Moreover, the ANs were higher for systems with deprotonated GA. This was a result of the electrostatic interactions between the anionic GA and the cationic QAILS polar head, corroborated by the CNs of the deprotonated moieties being lower at the micelle center. This increased the surface area along with the apolar regions of GA in the hydrophobic micelle cores, leading to micelle swelling. Despite this, these moieties were not completely removed from the apolar regions of the QAILS, as shown by the CNs larger than 0.

Overall, this deprotonation of GA gave rise to more electrostatic interactions with the QAILS cation, but also rendered it more polar (**Figure S3**), thus decreasing its presence in the QAILS-rich phase as the pH effect progressed. This was translated into phase separation for $[N_{4,4,4,14}]Cl$ and

partition at the outer side of the micelle surface for $[N_{1,1,1,14}]Cl$. It is also important to note that these values are, in certain systems, lower than the experimental counterparts, as we are dealing with PW in these CG simulations. The use of the PW CG model commonly yields smaller aggregates when compared with the regular martini water model counterpart.[87]

The impact of GA in similar QAILS surfactants was previously reported. Heins et al. published an increase of the AN in $[N_{1,1,1,16}]Br$ from 103 to 118 by adding 0.2% of GA, with GA being one of the phenolic acids inducing larger micelle swelling.[88]

The carboxylic and hydroxylic RDF profiles with the polar QAILS heads (micelle surface) were used to further confirm the above results as shown in **Figure S7**. The RDFs prove the effect of the GA protonation state in the interaction balance with the QAILS cationic head. For all systems the carboxylic moiety of Deprot. GA (-1) exhibited higher RDF intensity peaks, reflecting more electrostatic interactions with the QAILS charged region. When the hydroxylic moiety was also deprotonated, Deprot. GA (-3), the same tendency was observed, displaying this region with almost identical RDF intensity peaks as the carboxylic moiety. Thus, the hydroxylic region, even if deprotonated, was beyond the QAILS charged center compared with the carboxylic moiety. Moreover, since the ammonium charge is shielded by the butyl alkyl chains in $[N_{4,4,4,14}]^+$ and $[N_{4,4,4,4}]^+$, the hydroxylic moiety was placed beyond the QAILS cation.

It must be noted that the proximity of the deprotonated moieties of GA, both carboxylic and hydroxylic, to the QAILS ammonium charge can induce an ion-exchange mechanism. Since the GA was arranged close to the charged QAILS moieties (**Figure S7**), the effect of this proximity in the chloride counter anions can be assessed. The ion-exchange mechanism is discussed in detail in Section B of the SI.

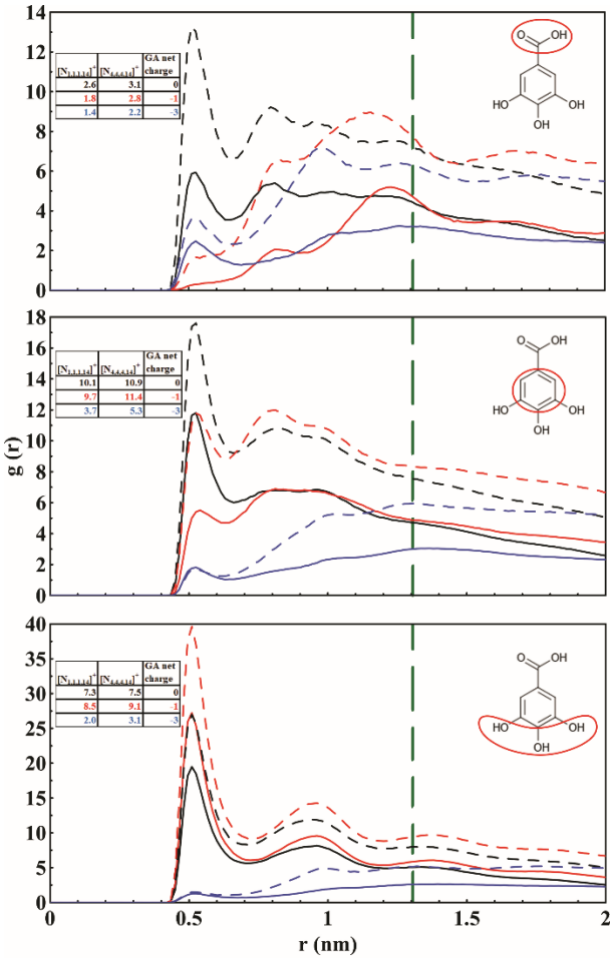

Figure 7. RDF profiles for (**Table S1**: systems 5-7, 12-14) $[N_{4,4,4,14}]^+$ (dashed lines) and $[N_{1,1,1,14}]^+$ (solid lines) aqueous solutions with GA. The QAILS penultimate bead was used as a reference and each GA selected group (carboxylic acid, aromatic ring, hydroxylic) as the selection (insets). Systems containing Prot. GA are depicted in black, Deprot. GA (-1) in red and Deprot. GA (-3) in blue. The micelle surface (at 1.31 nm) is illustrated by a green dashed line. CNs are shown aside the corresponding profile. CNs were obtained at r ≈ 0.51 nm (first peak).

4. Conclusions

This study aimed to enhance our understanding of micellar and hydrotropic solubilization mechanisms using aqueous solutions of quaternary ammonium ionic liquids and salts as the solubilizers and GA as the model solute. A molecular dynamics computational approach was used to foster our understanding on the underlying molecular interactions driving these solvation mechanisms. A new CG model for GA based on the MARTINI FF was developed to tackle the phase behaviour and to be able to capture the physico-chemical properties of this biomolecule. A

critical view into the role played by three different quaternary ammoniums in aqueous solutions was carried out, covering from the surfactant to hydrotrope like behaviours. Furthermore, different GA protonation states were evaluated to take into account the effect of the pH.

The effect of the pH covered in this computational study, indicated that dispersive interactions between the QAILS and GA are generally the driving force in the GA solubilization. Nonetheless, electrostatic interactions played also a significant role when GA was deprotonated, changing the placement of the GA in the micelle and its solvation mechanism. Interestingly, the results suggest that at high pH values ion exchange could take place with the formation of new QAILS with gallate as anion. The hydrotropic mechanism seen in $[N_{4,4,4,4}]Cl$ corroborates recent models based on the formation of a hydrotrope-solute aggregates driven by dispersive forces.

This methodology is easily applicable to the study of other poorly soluble molecules and the respective solubilizing/extracting candidates, as it simply requires the development and validation of CG models of the desired molecules, or the use of already existing ones, and parameter tuning. These results can complement experimental works in predicting outcomes in similar conditions as well as assist in explaining the molecular mechanisms driving phase transition phenomena. Ultimately, a quick screening of molecular candidates for various applications could be possible.

Acknowledgments

This work was developed within the scope of the project CICECO-Aveiro Institute of Materials, UIDB/50011/2020 & UIDP/50011/2020, financed by national funds through the FCT/MEC and when appropriate co-financed by FEDER under the PT2020 Partnership Agreement. The authors acknowledge the research contract under the project CENTRO-01-0145-FEDER-000005: SusPhotoSolutions: Soluções Fotovoltaicas Sustentáveis. N.S. would like to acknowledge financial support from the BATRE-ARES project (ERA-MIN/0001/2015) funded by ADEME and FCT. G. Pérez-Sánchez and N. Schaeffer acknowledge the national funds (OE), through FCT – Fundação para a Ciência e a Tecnologia, I.P., in the scope of the framework contract foreseen in the numbers 4, 5 and 6 of the article 23, of the Decree-Law 57/2016, of August 29, changed by Law 57/2017, of July 19.

References

1 S. M. Abuzar, S. M. Hyun, J. H. Kim, H. J. Park, M. S. Kim, J. S. Park and S. J. Hwang, Enhancing the solubility and bioavailability of poorly water-soluble drugs using supercritical antisolvent (SAS) process, *Int. J. Pharm.*, 2018, **538**, 1–13.

2 H. Mahmood and M. Moniruzzaman, Recent Advances of Using Ionic Liquids for Biopolymer Extraction and Processing, *Biotechnol. J.*, 2019, **14**, 1900072.

3 S. L. Baker, A. Munasinghe, B. Kaupbayeva, N. Rebecca Kang, M. Certiat, H. Murata, K. Matyjaszewski, P. Lin, C. M. Colina and A. J. Russell, Transforming protein-polymer conjugate purification by tuning protein solubility, *Nat. Commun.*, , DOI:10.1038/s41467-019-12612-9.

4 V. P. Torchilin, *Pharm. Res.*, 2007, 24, 1–16.

5 J. J. Booth, S. Abbott and S. Shimizu, Mechanism of Hydrophobic Drug Solubilization by Small Molecule Hydrotropes, *J. Phys. Chem. B*, 2012, **116**, 14915–14921.

6 N. Seedher and M. Kanojia, Co-solvent solubilization of some poorly-soluble antidiabetic drugs Solubilization antidiabetic drugs, *Pharm. Dev. Technol.*, 2009, **14**, 185–192.

7 T. Tadros, in *Colloid and Interface Science in Pharmaceutical Research and Development*, Elsevier Inc., 2014, pp. 29–54.

8 T. K. Hodgdon and E. W. Kaler, *Curr. Opin. Colloid Interface Sci.*, 2007, 12, 121–128.

9 S. Shimizu and N. Matubayasi, *Phys. Chem. Chem. Phys.*, 2017, 19, 23597–23605.

10 Z. Vinarov, V. Katev, D. Radeva, S. Tcholakova and N. D. Denkov, Micellar solubilization of poorly water-soluble drugs: effect of surfactant and solubilizate molecular structure, *Drug Dev. Ind. Pharm.*, 2018, **44**, 677–686.

11 D. O. Abranches, J. Benfica, B. P. Soares, A. Leal-Duaso, T. E. nia Sintra, E. sabet Pires, S. P. Pinho, S. Shimizu and J. A. P Coutinho, Unveiling the mechanism of hydrotropy: evidence for water-mediated aggregation of hydrotropes around the solute † ‡ ChemComm COMMUNICATION, *Chem. Commun*, 2020, **56**, 7143.

12 L. Y. Zakharova, T. N. Pashirova, A. R. Fernandes, S. Doktorovova, C. Martins-Gomes, A. M. Silva and E. B. Souto, in *Organic Materials as Smart Nanocarriers for Drug Delivery*, Elsevier, 2018, pp. 601–618.

13 S. H. Park and H. K. Choi, The effects of surfactants on the dissolution profiles of poorly

water-soluble acidic drugs, *Int. J. Pharm.*, 2006, **321**, 35–41.

14 S. Kumar, S. Singh, A. Bhadoria, K. Parikh, S. K. Yadav, S. Kumar and V. K. Aswal, Self-Assembly in Aqueous Oppositely Charged Gemini Surfactants: A Correlation between Morphology and Solubilization Efficacy, *J. Phys. Chem. B*, 2017, **121**, 8756–8766.

15 A. F. M. Cláudio, M. C. Neves, K. Shimizu, J. N. Canongia Lopes, M. G. Freire and J. A. P. Coutinho, The magic of aqueous solutions of ionic liquids: ionic liquids as a powerful class of catanionic hydrotropes, *Green Chem.*, 2015, **17**, 3948–3963.

16 T. E. Sintra, K. Shimizu, S. P. M. Ventura, S. Shimizu, J. N. Canongia Lopes and J. A. P. Coutinho, Enhanced dissolution of ibuprofen using ionic liquids as catanionic hydrotropes, *Phys. Chem. Chem. Phys.*, 2018, **20**, 2094–2103.

17 O. A. Chat, M. H. Najar, M. A. Mir, G. M. Rather and A. A. Dar, Effects of surfactant micelles on solubilization and DPPH radical scavenging activity of Rutin, *J. Colloid Interface Sci.*, 2011, **355**, 140–149.

18 I. Ullah, M. K. Baloch, I. Ullah and M. Mustaqeem, Enhancement in aqueous solubility of Mefenamic acid using micellar solutions of various surfactants, *J. Solution Chem.*, 2014, **43**, 1360–1373.

19 E. I. Gkaniatsou, C. N. Banti, N. Kourkoumelis, S. Skoulika, M. Manoli, A. J. Tasiopoulos and S. K. Hadjikakou, Novel mixed metal Ag(I)-Sb(III)-metallotherapeutics of the NSAIDs, aspirin and salicylic acid: Enhancement of their solubility and bioactivity by using the surfactant CTAB, *J. Inorg. Biochem.*, 2015, **150**, 108–119.

20 M. Moradi, Y. Yamini, A. Esrafili and S. Seidi, Application of surfactant assisted dispersive liquid-liquid microextraction for sample preparation of chlorophenols in water samples, *Talanta*, 2010, **82**, 1864–1869.

21 L. Wang and J. P. Stegemann, Extraction of high quality RNA from polysaccharide matrices using cetlytrimethylammonium bromide, *Biomaterials*, 2010, **31**, 1612–1618.

22 R. de C. S. Sousa, M. M. Pereira, M. G. Freire and J. A. P. Coutinho, Evaluation of the effect of ionic liquids as adjuvants in polymer-based aqueous biphasic systems using biomolecules as molecular probes, *Sep. Purif. Technol.*, 2018, **196**, 244–253.

23 F. A. E Silva, M. Caban, M. Kholany, P. Stepnowski, J. A. P. Coutinho and S. P. M. Ventura, Recovery of Nonsteroidal Anti-Inflammatory Drugs from Wastes Using Ionic-Liquid-Based Three-Phase Partitioning Systems, *ACS Sustain. Chem. Eng.*, 2018, **6**, 4574–

4585.

24 A. F. M. Cláudio, A. M. Ferreira, C. S. R. Freire, A. J. D. Silvestre, M. G. Freire and J. A. P. Coutinho, in *Separation and Purification Technology*, 2012, vol. 97, pp. 142–149.

25 M. Collinet-Fressancourt, L. Leclercq, P. Bauduin, J. M. Aubry and V. Nardello-Rataj, Counter anion effect on the self-aggregation of dimethyl-di-N-octylammonium cation: A dual behavior between hydrotropes and surfactants, *J. Phys. Chem. B*, 2011, **115**, 11619–11630.

26 V. Srinivas and D. Balasubramanian, When does the switch from hydrotropy to micellar behavior occur?, *Langmuir*, 1998, **14**, 6658–6661.

27 G. Perez-Sanchez, F. A. Vicente, N. Schaeffer, I. S. Cardoso, S. P. M. Ventura, M. Jorge and J. A. P. Coutinho, Rationalizing the Phase Behavior of Triblock-Copolymers Through Experiments and Molecular Simulations, *J. Phys. Chem. C*, 2019, **123**, 21224–21236.

28 F. A. E Silva, M. Caban, P. Stepnowski, J. A. P. Coutinho and S. P. M. Ventura, Recovery of ibuprofen from pharmaceutical wastes using ionic liquids, *Green Chem.*, 2016, **18**, 3749–3757.

29 K. Häckl, A. Mühlbauer, J. F. Ontiveros, S. Marinkovic, B. Estrine, W. Kunz and V. Nardello-Rataj, Carnitine alkyl ester bromides as novel biosourced ionic liquids, cationic hydrotropes and surfactants, *J. Colloid Interface Sci.*, 2018, **511**, 165–173.

30 N. Schaeffer, H. Passos, M. Gras, V. Mogilireddy, J. P. Leal, G. Pérez-Sánchez, J. R. B. Gomes, I. Billard, N. Papaiconomou and J. A. P. Coutinho, Mechanism of ionic-liquid-based acidic aqueous biphasic system formation, *Phys. Chem. Chem. Phys.*, 2018, **20**, 9838–9846.

31 H. Abe, A. Takeshita, H. Sudo, K. Akiyama and H. Kishimura, CO 2 Capture at Room Temperature and Ambient Pressure: Isomer Effect in Room Temperature Ionic Liquid/Propanol Solutions, *Green Sustain. Chem.*, 2016, **6**, 116–124.

32 M. L. P. Le, F. Alloin, P. Strobel, J.-C. Leprêtre, C. Pérez del Valle and P. Judeinstein, Structure−Properties Relationships of Lithium Electrolytes Based on Ionic Liquid, *J. Phys. Chem. B*, 2010, **114**, 894–903.

33 K. Fumino, A. Wulf and R. Ludwig, Hydrogen Bonding in Protic Ionic Liquids: Reminiscent of Water, *Angew. Chemie Int. Ed.*, 2009, **48**, 3184–3186.

34 T. Marino, A. Galano and N. Russo, Radical Scavenging Ability of Gallic Acid toward OH

and OOH Radicals. Reaction Mechanism and Rate Constants from the Density Functional Theory, *J. Phys. Chem. B*, 2014, **118**, 10380–10389.

35 M. L. Vueba, M. E. Pina and L. A. E. Batista De Carvalho, Conformational stability of ibuprofen: Assessed by DFT calculations and optical vibrational spectroscopy, *J. Pharm. Sci.*, 2008, **97**, 845–859.

36 J. K. Shah and E. J. Maginn, A Monte Carlo simulation study of the ionic liquid 1-n-butyl-3- methylimidazolium hexafluorophosphate: Liquid structure, volumetric properties and infinite dilution solution thermodynamics of CO2, *Fluid Phase Equilib.*, 2004, **222**–**223**, 195–203.

37 C. Verma, I. B. Obot, I. Bahadur, E. S. M. Sherif and E. E. Ebenso, Choline based ionic liquids as sustainable corrosion inhibitors on mild steel surface in acidic medium: Gravimetric, electrochemical, surface morphology, DFT and Monte Carlo simulation studies, *Appl. Surf. Sci.*, 2018, **457**, 134–149.

38 L. L. Liao, S. Mo, H. Q. Luo and N. B. Li, Longan seed and peel as environmentally friendly corrosion inhibitor for mild steel in acid solution: Experimental and theoretical studies, *J. Colloid Interface Sci.*, 2017, **499**, 110–119.

39 D. Bahamon, L. Carro, S. Guri and L. F. Vega, Computational study of ibuprofen removal from water by adsorption in realistic activated carbons, *J. Colloid Interface Sci.*, 2017, **498**, 323–334.

40 K. Shimizu, A. A. H. Pádua and J. N. Canongia Lopes, Nanostructure of Trialkylmethylammonium Bistriflamide Ionic Liquids Studied by Molecular Dynamics, *J. Phys. Chem. B*, 2010, **114**, 15635–15641.

41 C. Cappelli, B. Mennucci and S. Monti, Environmental effects on the spectroscopic properties of gallic acid: A combined classical and quantum mechanical study, *J. Phys. Chem. A*, 2005, **109**, 1933–1943.

42 M. D. Chatzidaki, K. D. Papavasileiou, M. G. Papadopoulos and A. Xenakis, Reverse Micelles As Antioxidant Carriers: An Experimental and Molecular Dynamics Study, *Langmuir*, 2017, **33**, 5077–5085.

43 P. Prakash, A. Sayyed-Ahmad, Y. Zhou, D. E. Volk, D. G. Gorenstein, E. Dial, L. M. Lichtenberger and A. A. Gorfe, Aggregation behavior of ibuprofen, cholic acid and dodecylphosphocholine micelles, *Biochim. Biophys. Acta - Biomembr.*, 2012, **1818**, 3040–

3047.

44 C. Dai, M. Du, Y. Liu, S. Wang, J. Zhao, A. Chen, D. Peng and M. Zhao, Aggregation Behavior of Long-Chain Piperidinium Ionic Liquids in Ethylammonium Nitrate, *Molecules*, 2014, **19**, 20157–20169.

45 D. Xiang, H. Liu, L. Yang, Y. Liang, J. Zhu, Z. Lu, Y. Hou and M. Yang, From Molecular-Level Organization to Nanoscale Positioning: Synergetic Ligand Effect on the Synthesis of Hybrid Nanostructures, *Adv. Funct. Mater.*, 2017, **27**, 1703006.

46 C. Long, L. Zhang and Y. Qian, Mesoscale simulation of drug molecules distribution in the matrix of solid lipid microparticles (SLM), *Chem. Eng. J.*, 2006, **119**, 99–106.

47 R. O. Jones, Density functional theory: Its origins, rise to prominence, and future, *Rev. Mod. Phys.*, 2015, **87**, 897–923.

48 S. A. Hollingsworth and R. O. Dror, Molecular Dynamics Simulation for All, *Neuron*, 2018, **99**, 1129–1143.

49 S. J. Marrink, H. J. Risselada, S. Yefimov, D. P. Tieleman and A. H. De Vries, The MARTINI force field: Coarse grained model for biomolecular simulations, *J. Phys. Chem. B*, 2007, **111**, 7812–7824.

50 N. Schaeffer, G. Pérez-Sánchez, H. Passos, J. R. B. Gomes, N. Papaiconomou and J. A. P. Coutinho, Mechanisms of phase separation in temperature-responsive acidic aqueous biphasic systems, *Phys. Chem. Chem. Phys.*, 2019, **21**, 7462–7473.

51 G. I. Hidalgo and M. P. Almajano, Red fruits: Extraction of antioxidants, phenolic content, and radical scavenging determination: A review, *Antioxidants*, 2017, **6**, 7.

52 J. D. Everette, Q. M. Bryant, A. M. Green, Y. A. Abbey, G. W. Wangila and R. B. Walker, Thorough study of reactivity of various compound classes toward the folin-Ciocalteu reagent, *J. Agric. Food Chem.*, 2010, **58**, 8139–8144.

53 K. R. Raghi, D. R. Sherin, M. J. Saumya, P. S. Arun, V. N. Sobha and T. K. Manojkumar, Computational study of molecular electrostatic potential, docking and dynamics simulations of gallic acid derivatives as ABL inhibitors, *Comput. Biol. Chem.*, 2018, **74**, 239–246.

54 L. Lespade, Ab initio molecular dynamics of electron transfer from gallic acid to small radicals: A comparative study between hydroxyl and nitrogen dioxide radicals, *Comput. Theor. Chem.*, 2018, **1135**, 6–10.

55 M. J. Abraham, T. Murtola, R. Schulz, S. Páll, J. C. Smith, B. Hess and E. Lindahl,

GROMACS: High performance molecular simulations through multi-level parallelism from laptops to supercomputers, *SoftwareX*, 2015, **1**–**2**, 19–25.

56 R. W. Hockney, S. P. Goel and J. W. Eastwood, Quiet high-resolution computer models of a plasma, *J. Comput. Phys.*, 1974, **14**, 148–158.

57 T. Darden, D. York and L. Pedersen, Particle mesh Ewald: An N·log(N) method for Ewald sums in large systems, *J. Chem. Phys.*, 1993, **98**, 10089–10092.

58 G. Bussi, D. Donadio and M. Parrinello, Canonical sampling through velocity rescaling, *J. Chem. Phys.*, 2007, **126**, 014101.

59 M. Parrinello and A. Rahman, Polymorphic transitions in single crystals: A new molecular dynamics method, *J. Appl. Phys.*, 1981, **52**, 7182–7190.

60 B. Hess, H. Bekker, H. J. C. Berendsen and J. G. E. M. Fraaije, LINCS: A linear constraint solver for molecular simulations, *J. Comput. Chem.*, 1997, **18**, 1463–1472.

61 G. Pérez-Sánchez, J. R. B. Gomes and M. Jorge, Modeling self-assembly of silica/surfactant mesostructures in the templated synthesis of nanoporous solids, *Langmuir*, 2013, **29**, 2387–2396.

62 PubChem, Open Chemistry database. PubChem Substance and Compound database, https://pubchem.ncbi.nlm.nih.gov/.

63 Chemicalize was used for generation of gallic acid speciation properties (May 2020), https://chemicalize.com/ developed by ChemAxon, https://www.chemaxon.com.

64 W. Humphrey, A. Dalke and K. Schulten, VMD: Visual molecular dynamics, *J. Mol. Graph.*, 1996, **14**, 33–38.

65 M. Jorge, Molecular dynamics simulation of self-assembly of n-decyltrimethylammonium bromide micelles, *Langmuir*, 2008, **24**, 5714–5725.

66 J. Hoshen and R. Kopelman, Percolation and cluster distribution. I. Cluster multiple labeling technique and critical concentration algorithm, *Phys. Rev. B*, 1976, **14**, 3438–3445.

67 M. Brehm and B. Kirchner, TRAVIS - A Free Analyzer and Visualizer for Monte Carlo and Molecular Dynamics Trajectories, *J. Chem. Inf. Model.*, 2011, **51**, 2007–2023.

68 W. L. Jorgensen, D. S. Maxwell and J. Tirado-Rives, Development and testing of the OPLS all-atom force field on conformational energetics and properties of organic liquids, *J. Am. Chem. Soc.*, 1996, **118**, 11225–11236.

69 H. J. C. Berendsen, J. R. Grigera and T. P. Straatsma, The missing term in effective pair

potentials, *J. Phys. Chem.*, 1987, **91**, 6269–6271.

70 C. Lee, W. Yang and R. G. Parr, Development of the Colle-Salvetti correlation-energy formula into a functional of the electron density, *Phys. Rev. B*, 1988, **37**, 785–789.

71 C. M. Breneman and K. B. Wiberg, Determining atom-centered monopoles from molecular electrostatic potentials. The need for high sampling density in formamide conformational analysis, *J. Comput. Chem.*, 1990, **11**, 361–373.

72 M. J. Frisch, G. W. Trucks, H. B. Schlegel, G. E. Scuseria, M. A. Robb, J. R. Cheeseman, G. Scalmani, V. Barone, G. A. Petersson, H. Nakatsuji, X. Li, M. Caricato, A. Marenich, J. Bloino, B. G. Janesko, R. Gomperts, B. Mennucci, H. P. Hratchian, J. V. Ort and D. J. Fox, *Gaussian 09 (revision D.01)*, Gaussian Inc., Wallingford, CT, 2009.

73 J. L. Beltrán, N. Sanli, G. Fonrodona, D. Barrón, G. Özkan and J. Barbosa, Spectrophotometric, potentiometric and chromatographic pKa values of polyphenolic acids in water and acetonitrile-water media, *Anal. Chim. Acta*, 2003, **484**, 253–264.

74 V. Patel, N. Dharaiya, D. Ray, V. K. Aswal and P. Bahadur, pH controlled size/shape in CTAB micelles with solubilized polar additives: A viscometry, scattering and spectral evaluation, *Colloids Surfaces A Physicochem. Eng. Asp.*, 2014, **455**, 67–75.

75 C. D. Umeasiegbu, V. Balakotaiah and R. Krishnamoorti, pH-Induced Re-entrant Microstructural Transitions in Cationic Surfactant-Hydrotrope Mixtures, *Langmuir*, 2016, **32**, 655–663.

76 W. F. D. Bennett, A. W. Chen, S. Donnini, G. Groenhof and D. P. Tieleman, Constant pH simulations with the coarse-grained MARTINI model — Application to oleic acid aggregates, *Can. J. Chem.*, 2013, **91**, 839–846.

77 L. Y. Zakharova, T. N. Pashirova, S. Doktorovova, A. R. Fernandes, E. Sanchez-Lopez, A. M. Silva, S. B. Souto and E. B. Souto, Cationic surfactants: Self-assembly, structure-activity correlation and their biological applications, *Int. J. Mol. Sci.*, 2019, **20**, 5534.

78 K. Schwarz, E. N. Frankel and J. B. German, Partition behaviour of antioxidative phenolic compounds in heterophasic systems, *Lipid/Fett*, 1996, **98**, 115–121.

79 S. A. Buckingham, C. J. Garvey and G. G. Warr, Effect of head-group size on micellization and phase behavior in quaternary ammonium surfactant systems, *J. Phys. Chem.*, 1993, **97**, 10236–10244.

80 G. G. Warr, T. N. Zemb and M. Drifford, Liquid-liquid phase separation in cationic micellar

solutions, *J. Phys. Chem.*, 1990, **94**, 3086–3092.

81 D. Lombardo, M. A. Kiselev, S. Magazù and P. Calandra, Amphiphiles Self-Assembly: Basic Concepts and Future Perspectives of Supramolecular Approaches, *Adv. Condens. Matter Phys.*, 2015, **2015**, 1–22.

82 J. Israelachvili, *Intermolecular and Surface Forces*, Elsevier Inc., 2011.

83 Z. J. Yu and G. Xu, Physicochemical properties of aqueous mixtures of tetrabutylammonium bromide and anionic surfactants. 1. Temperature-induced micellar growth and cloud point phenomenon, *J. Phys. Chem.*, 1989, **93**, 7441–7445.

84 Kabir-ud-Din, D. Sharma, Z. A. Khan, V. K. Aswal and S. Kumar, Clouding phenomenon and SANS studies on tetra-n-butylammonium dodecylsulfate micellar solutions in the absence and presence of salts, *J. Colloid Interface Sci.*, 2006, **302**, 315–321.

85 S. Shimizu and N. Matubayasi, The origin of cooperative solubilisation by hydrotropes, *Phys. Chem. Chem. Phys.*, 2016, **18**, 25621–25628.

86 J. J. Booth, M. Omar, S. Abbott and S. Shimizu, Hydrotrope accumulation around the drug: The driving force for solubilization and minimum hydrotrope concentration for nicotinamide and urea, *Phys. Chem. Chem. Phys.*, 2015, **17**, 8028–8037.

87 J. F. Kraft, M. Vestergaard, B. Schiøtt and L. Thøgersen, Modeling the self-assembly and stability of DHPC micelles using atomic resolution and coarse grained MD simulations, *J. Chem. Theory Comput.*, 2012, **8**, 1556–1569.

88 A. Heins, V. M. Garamus, B. Steffen, H. Stöckmann and K. Schwarz, Impact of Phenolic Antioxidants on Structural Properties of Micellar Solutions, *Food Biophys.*, 2006, **1**, 189–201.

Graphical Abstract